Galaxy alignments from multiple angles

Fortuna, M.C.

4 KiDS-1000: weak lensing and intrinsic alignment around luminous red galaxies

M.C Fortuna, *H. Hoekstra, A.Dvornik*

We study the properties of the Luminous Red Galaxies (LRGs) selected from the 4th data release of the Kilo Degree Survey (KiDS-1000) via galaxy-galaxy lensing of the background galaxies from KiDS-1000. We use a halo model formalism to model our measurements and obtain estimates of the halo masses and the satellite fractions of the LRGs. We use these to interpret the intrinsic alignment (IA) measurements in Fortuna et al. (2021b), who studied the tendency of the LRGs to point in the direction of other LRGs, via the galaxy shape-galaxy position correlation. Here, we directly link the observed IA of the (central) galaxy to the mass of the hosting halo, which is expected to be a fundamental quantity in establishing the alignment, and find that the dependence of the IA amplitude on halo mass is described well by a single power law. We also find that both red and blue galaxies from the source sample associated with the LRGs are oriented randomly with respect to the LRGs.

4.1 Introduction

The intrinsic alignment (IA) of galaxies, defined as the tendency of galaxies to point in a coherent direction, has gained attention in the last two decades as an important contaminant to lensing (Heavens et al. 2000; Crittenden et al. 2001; Kirk et al. 2010; Krause et al. 2016, among others). N-body simulations have explored the origin of the triaxility and angular momentum of dark matter haloes, and how they orient their major axis in the direction of matter overdensities, finding that the orientation also depends on the environment and the location on the large scale structure (Dubinski 1992; Croft & Metzler 2000; Hopkins et al. 2005; Hahn et al. 2007; Lee et al. 2008; Forero-Romero et al. 2014). Models of galaxy alignment predict that the galaxy inherits the orientation of its major axis from the orientation of the parent halo: such a relation is expected to be primarily sourced by the effect of tidal fields during galaxy formation (Catelan et al. 2001). These models predict a dichotomy in the alignment of elliptical, pressure-supported galaxies, and disc-like, rotationally supported galaxies (e.g. Catelan et al. 2001; Hirata & Seljak 2004), in agreement with results from observations (Hirata et al. 2007; Faltenbacher et al. 2009; Joachimi et al. 2011; Blazek et al. 2011; Singh et al. 2015; Johnston et al. 2019; Mandelbaum et al. 2011).

Observations have shown that luminous red galaxies (LRGs) are the main source of IA and that the dependence on luminosity can be described by a power law (Hirata et al. 2007; Joachimi et al. 2011; Singh et al. 2015). Fortuna et al. (2021b) extended observational constraints on the IA amplitude to samples of LRGs with significantly lower luminosities compared to previous studies, and found that the dependence with luminosity is shallower compared to the high-L samples. This points toward a more complex behaviour in the luminosity-alignment relation.

The relation between luminosity and halo mass itself is complex. Hence, a simple dependence with halo mass, as predicted by models of IA (Xia et al. 2017; Piras et al. 2018), would result in a complex dependence of the IA signal with luminosity. It is therefore interesting to explore the observational link between the IA of galaxies and the mass of the hosting halo. This could simplify the modelling and help generate synthetic galaxy catalogues that reproduce the observed IA using halo catalogues from N-body simulations (e.g. Carretero et al. 2017). A direct measure of IA as a function of halo mass avoids the intermediate step of calibrating IA on secondary galaxy properties that are not directly responsible for the alignment mechanism

and that have non-negligible scatter.

In this paper we determine the average halo mass for the samples used in Fortuna et al. (2021b), direct linking their IA signal and their halo mass. Singh et al. (2015); van Uitert & Joachimi (2017) and Piras et al. (2018) have addressed the same question using higher luminosity/higher mass samples, finding a single power law relation for the IA dependence on halo mass. Here, we extend the analysis to the faint-end, where the IA dependence on luminosity changes its slope. This allows us to address the question whether the observed flattening in the IA amplitude is a consequence of a similar flattening in the halo mass-luminosity relation.

To measure the halo masses, we employ weak gravitational lensing: light bundles of the distant galaxies are deflected by the matter distribution along the line of sight, which leads to an apparent correlation between the shape of a background galaxy (source) and the position of a foreground galaxy (lens). This galaxy-galaxy lensing (GGL) signal is an important tool to investigate the dark matter distribution around galaxies (e.g. Hoekstra et al. 2005; Mandelbaum et al. 2006; Velander et al. 2014; Miyatake et al. 2015; van Uitert et al. 2015; Dvornik et al. 2020; Bilicki et al. 2021).

In this paper, we use the halo model to connect the statistical properties of dark matter haloes to those of the galaxies. It is an analytical approach to predict observable quantities based on the link between the galaxy occupation statistics, the abundance, and the clustering of dark matter (Seljak 2000; Ma & Fry 2000; Cooray & Sheth 2002).

In this study, the lens sample consists of LRGs in the footprint of the 4th data release of KiDS (KiDS-1000, Kuijken et al. 2019), which were selected via a variation of the redMagiC algorithm (Rykoff et al. 2014), as presented in Vakili et al. (2020). To measure the lensing signal, we use the source sample presented in Giblin et al. (2021).

LRGs are typically the central galaxies in massive haloes, and are responsible for the alignment at large scales. The alignment at small scales is sourced by satellite galaxies: the intra-halo tidal fields align the satellites in a torquing mechanism that leads to a net radial alignment signal towards the halo centre (Pereira et al. 2008). In this paper, we investigate this signal by determining the alignment of galaxies in the source sample. These are selected to be physically close to the LRGs, so that the LRG can be considered a proxy for the halo centre. To do so, we employ an estimator that is similar to the one used GGL, following the approach presented in Blazek et al. (2012). When measuring the signal, we account for the lensing contamination and the lensing dilution that occurs between galaxies that are

physically associated. The IA of the sources presented here is complementary to the study of the IA signal in Fortuna et al. (2021b), who looked at the alignment signal of the LRG sample at large scales. Here, we constrain the small scale signal ($r_{\rm p} < 10h^{-1}{\rm Mpc}$) sourced by non-LRG galaxies. These results can thus be used to inform models such as the halo model.

The paper is organised as follows: in Sect. 4.2 we present the data employed in this work; in Sect. 4.3 we introduce the estimator used to measure the signal, while in Sect. 4.4 we present the model framework we use to interpret the measurements. In Sect. 4.5 we detail the fitting procedure and in Sect. 4.6 and Sect. 4.7 we present our results. In Sect. 4.8 we draw our conclusions.

Throughout the paper, we assume a flat ΛCDM cosmology with $h = 0.7, \Omega_{\rm m} = 0.25, \Omega_{\rm b} = 0.044, \sigma_8 = 0.8$ and $n_{\rm s} = 0.96$. Absolute magnitudes are computed assuming $h = 1$.

4.2 Data

The data employed in this work are collected by the Kilo Degree Survey (KiDS), a multi-band imaging survey that has mapped 1350 deg^2 of the sky, divided in two equally sized patches, one in the equatorial region and one in the Southern hemisphere. The latest data release (DR4, hereafter KiDS-1000) covers 1006 deg^2 and provides high quality images in the *ugri* bands, obtained on the VLT Survey Telescope (VST; Capaccioli et al. 2012) with the OmegaCAM instrument (Kuijken 2011). By survey design, the best images are provided in the $r-$band, where the mean magnitude limit is $r \sim 25$ (5σ in a $2''$ aperture), and thus we will always refer to the $r-$band images in the rest of this work. Five infrared bands, $ZYJHK_{\rm s}$, obtained from the companion survey VISTA Kilo-degree INfrared Galaxy survey (VIKING; Edge et al. 2013), complement the data, allowing for a robust photometric redshift calibration (Wright et al. 2019; Hildebrandt et al. 2020).

4.2.1 The lens sample

The LRG sample is selected from KiDS-1000 using a variation of the redMagiC algorithm (Rykoff et al. 2014), as presented in Vakili et al. (2019, 2020). Details of the sample properties can be found in Vakili et al. (2020). Here we summarise the most relevant ones. The sample is selected with a redshift-dependent magnitude cut to ensure a constant comoving number density. The parameter that regulates the selection is $m_r^{\rm pivot}(z)$, the char-

acteristic r-band magnitude of the Schechter (1976) function, assuming a faint-end slope $\alpha = 1$. The resulting luminous-threshold samples are defined by the ratio:

$$\frac{L}{L_{\rm pivot}(z)} = 10^{-0.4(m_r - m_{r,{\rm pivot}}(z))} \,, \tag{4.1}$$

where $m_r^{\rm pivot}(z)$ is evaluated using the EzGal (Mancone & Gonzalez 2012) implementation of Bruzual & Charlot (2003), assuming a Salpeter initial mass function (Chabrier 2003), a solar metallicity ($Z = 0.02$) and a single star formation burst at $z = 3$.

Two samples are obtained with the aforementioned strategy: a high luminosity ($L/L_{\rm pivot}(z) > 1$) and sparser sample ($\bar{n}_{\rm g} = 2.5 \times 10^{-4} h^3 {\rm Mpc}^{-3}$) named `luminous` sample and a denser ($\bar{n}_{\rm g} = 10^{-3} h^3 {\rm Mpc}^{-3}$) and less luminous one ($L/L_{\rm pivot}(z) > 0.5$), the `dense` sample. In this work, we follow Fortuna et al. (2021b) and use both samples for our analysis, but from the `dense` samples we removed the galaxies that are in common with the `luminous` sample. For a detailed explanation of why the two samples contain overlapping galaxies, we refer to Fortuna et al. (2021b). We also adopt the same luminosity-binning scheme as Fortuna et al. (2021b), with some minor variation as described in Sect. 4.6.

We quantify the scatter in the photometric-spectroscopic redshift relation using the scaled median absolute deviation of $(z_{\rm phot} - z_{\rm spec})/(1 + z_{\rm spec})$. This increases with redshift and it is tighter for the `luminous` sample. In particular, we find $\sigma_z = 0.0139$ for the `luminous` sample and $\sigma_z = 0.0146$ for the `dense` sample. This is also responsible for some overlap of the galaxy properties between the two samples, even when removing the overlapping galaxies.

The stellar masses and absolute magnitudes are obtained via LePhare (Arnouts & Ilbert 2011), assuming the stellar population synthesis model from Bruzual & Charlot (2003), the Chabrier (2003) initial mass function and Calzetti et al. (1994) dust-extinction law. We use the `MASS_BEST` output from LePhare as our best estimate of the mass to use for the point mass approximation (see Sect. 4.4). When computing the mean stellar mass per bin, we remove the galaxies for which the masses estimated as `MASS_MED` are flagged as bad (-99), indicating that the best fit was performed by a non-galaxy template[1].

[1]These galaxies are, however, used in the measurements, as our main focus is the luminosity-to-halo mass relation and the luminosity is robustly measured. We note that the change in the average mass is at the sub-percent level.

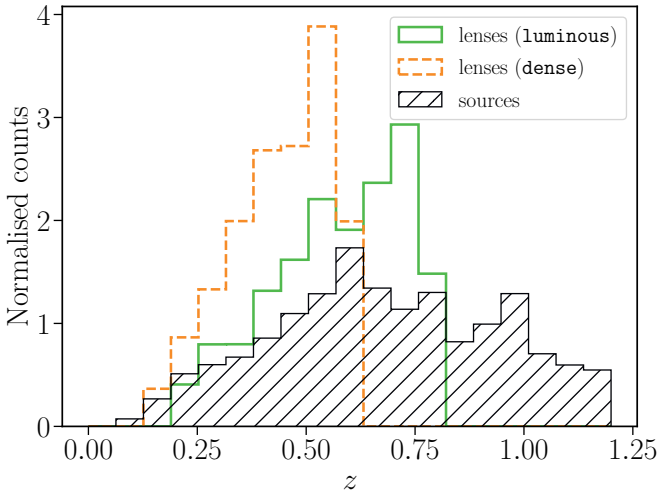

Figure 4.1: The photometric redshift distributions of the source and lens samples employed in the analysis. When computing the GGL signal, we only consider source galaxies at higher redshift than the lens, and with a minimum separation of $z_\epsilon = 0.2$.

We correct the absolute magnitudes for the passive evolution of the stellar population (e–correction). We use EzGal to compute it and follow the setup used in Vakili et al. (2020) to identify the limiting magnitude for the selection of the LRG candidates as described above.

4.2.2 The source sample

The shapes of our galaxies are computed via a self-calibrating version of *lens*fit (Miller et al. 2007, 2013; Fenech Conti et al. 2017; Kannawadi et al. 2019; Giblin et al. 2021)[2]. *lens*fit is a model-based algorithm that provides a measure of the ellipticity by fitting a PSF-convolved two-component bulge and disc model of a galaxy. It returns the ellipticity components $\epsilon = \epsilon_1 + i\epsilon_2$, with $|\epsilon| = (a-b)/(a+b)$, where a, b are, respectively, the major and minor axis. For each galaxy, the method returns also a weight, w_s, which accounts for the increase/decrease in the S/N due to the relative orientation of the galaxy with respect to the PSF and the overall S/N. Note that with this definition, the average ellipticity is an estimator of the shear, $\langle\epsilon\rangle = \gamma$.

The KiDS-1000 shear catalogue benefits from the improvement in the PSF treatment due to the available information provided by the *Gaia* mis-

[2]The catalogue is publicly available at `http://kids.strw.leidenuniv.nl/DR4/KiDS-1000_shearcatalogue.php`

sion (Gaia Collaboration et al. 2018). The shears are also calibrated to account for the multiplicative bias (m–bias) that arises as a further correlation between shear systematics: this is calibrated employing high fidelity image simulations based on deep images of the Cosmic Evolution Survey (COSMOS Scoville et al. 2007). We will discuss the m–bias again in Sec. 4.3, where we apply it to our lensing measurements. A full description of the catalogue and the systematic tests can be found in Giblin et al. (2021), while more details on the strategy to calibrate residual biases in described in Kannawadi et al. (2019).

The distributions of our photometric redshifts are illustrated in Fig. 4.1. These redshifts of the source galaxies are estimated based on deep spectroscopic catalogues that cover a sub-sample of the galaxies: these are then re-weighted using a self-organised map (SOM, Wright et al. 2020) to resemble the KiDS-1000 sample, and only sources that fill the SOM cells (a nine-dimensional magnitude-space volume) enter our final sample. The method is also validated by using a clustering–z algorithm. Details on the photometric redshift calibration can be found in Hildebrandt et al. (2021). We restrict our analysis to source galaxies in the redshift range $0.1 < z_{\rm s} < 1.2$, based on the available calibration of their photometric redshift via the SOM, where $z_{\rm s}$ indicates the photometric redshift of the source galaxy.

4.3 Measuring the signal

The GGL signal is quantified by the tangential distortion in the shapes of background galaxies (sources) induced by the mass distribution of the foreground galaxies (lenses) along the line-of-sight. As the distortion for a single lens galaxy is small and we lack information on the intrinsic shape of the background galaxy, we perform a statistical analysis of the signal encoded by a large number of lens-source galaxy pairs and measure the mean tangential shear around each lens as a function of lens-source galaxy projected separation, $\langle \gamma_{\rm t}(r_{\rm p}) \rangle$. This is a direct measure of the enclosed mass, as we will see later. Note that the S/N of the lensing signal around individual lenses is too small to be detected, and thus we average the signals of an ensemble of lenses. Here, we are implicitly assuming the weak lensing regime, so that the effective shear of a background galaxy can be approximated by the sum of the shears of the individual galaxies in the foreground. We measure the signal of both the `dense` and `luminous` samples in bins of luminosity.

For each source-lens pair, we measure the tangential component of the

ellipticity: indicating with ϕ the angle between the $x-$axis and the lens-source separation vector, and using the ellipticity definition introduced in Sec. 4.2.2, we have

$$\begin{bmatrix} \epsilon_{\rm t} \\ \epsilon_{\times} \end{bmatrix} = \begin{bmatrix} -\cos(2\phi) & -\sin(2\phi) \\ \sin(2\phi) & -\cos(2\phi) \end{bmatrix} \begin{bmatrix} \epsilon_1 \\ \epsilon_2 \end{bmatrix} \ . \tag{4.2}$$

Here, $\epsilon_{\times}$ is the cross-component of the ellipticity, which corresponds to a rotation of $45\,\deg$. The cross-component is an important test of residual systematics and in our measurements we always ensure that the cross-component is compatible with noise.

The ensemble average of the ellipticities of all the sources – which we remind the reader is an estimator of the shear – at projected separation $r_{\rm p}$ from the lens is directly related to the the amount of matter that we observe around a galaxy, which is quantified by the excess surface mass density (ESD) profile:

$$\Delta\Sigma(r_{\rm p}) = \bar{\Sigma}(< r_{\rm p}) - \Sigma(r_{\rm p}) = \gamma_{\rm t}(r_{\rm p})\,\Sigma_{\rm crit} \ . \tag{4.3}$$

The ESD is thus defined as the difference between the mean projected surface mass density enclosed in a projected radius $r_{\rm p}$ and the surface mass density at $r_{\rm p}$. The critical surface mass density is a geometrical factor defined as

$$\Sigma_{\rm crit} = \frac{c^2}{4\pi G(1+z_{\rm l})^2}\frac{D(z_{\rm s})}{D(z_{\rm l})D(z_{\rm l},z_{\rm s})} \ , \tag{4.4}$$

where the factor $(1+z_{\rm l})^2$ at the denominator accounts for our use of comoving units (see also Dvornik et al. 2018, Appendix C for a discussion on this term). Here, $z_{\rm l}$ ($z_{\rm s}$) is the redshift of the lens (source) galaxy, and $D(z_{\rm l})$, $D(z_{\rm s})$ and $D(z_{\rm l},z_{\rm s})$ are, respectively, the angular diameter distance to the lens, to the source and between the lens and the source galaxies.

As we rely on photometric redshifts, we need to integrate Eq. 4.4 for the redshift probability distributions of the source sample, $n(z_{\rm s})$, and the individual redshift probability distribution of each lens, $p(z_{\rm l})$. This provides an effective estimate of $\Sigma_{\rm crit}$:

$$\Sigma^{-1}_{\rm crit,eff} = \frac{4\pi G}{c^2}\int_0^{\infty}(1+z_{\rm l})^2 D(z_{\rm l})\left(\int_{z_{\rm l}}^{\infty}\frac{D(z_{\rm l},z_{\rm s})}{D(z_{\rm s})}n(z_{\rm s})\mathrm{d}z_{\rm s}\right)p(z_{\rm l})\mathrm{d}z_{\rm l} \ . \tag{4.5}$$

To model $p(z_{\rm l})$ we use a Gaussian centred on the photometric redshift of the given lens and with standard deviation given by the value of σ_z associated to the specific sample, as discussed in Sect. 4.2.1. The redshift probability

distribution of the source sample, $n(z_s)$, is instead obtained from the SOM as described in Sec. 4.2.2.

The lensing signal decreases as the distance between the lenses and the sources decreases (due to the $D(z_l, z_s)$ in Σ_{crit}^{-1}). In our case, while the lenses span a large range in redshift ($0.15 < z_l < 0.8$), the signal is limited by the source sample, for which we have robust redshift estimates only up to $z_s = 1.2$ (Wright et al. 2020). This means that our lensing efficiency peaks around $z_{ls} \sim 0.3$ and rapidly decreases as we approach high redshifts.

To each lens-source pair we also assign a weight determined by three components: a weight associated to the source sample, w_s, which down-weights the shears of the galaxies with low S/N, and that corresponds to the *lens*fit weight reported as `weight` in the KiDS-1000 shear catalogue (see Sect. 4.2.2); a weight associated to the lens galaxies, which is designed to remove residual correlations between the spatial galaxy number density and the survey observing conditions (Vakili et al. 2020); and a geometric term that down-weights lens-source pairs that are close in redshift, given by the square of the inverse critical mass surface density:

$$w_{ls,eff} = w_s w_l \left(\Sigma_{crit,eff}^{-1}\right)^2 . \tag{4.6}$$

Our estimator (here indicated with a hat) for the excess surface mass density thus reads:

$$\Delta\hat{\Sigma}_{ls}(r_p) = \left[\frac{\sum_{ls} w_{ls,eff}\ \epsilon_{t,s}\ \Sigma_{crit,eff}}{\sum_{ls} w_{ls,eff}}\right] \frac{1}{1+\bar{m}}\bigg|_{r_p} , \tag{4.7}$$

where we have included an average correction to the galaxy shear obtained from dedicated simulations, which quantifies the residual multiplicative bias in the estimate shear due to the presence of noise and blending in the images. The $m-$bias is a function of redshift (Kannawadi et al. 2019): here we rely on the calibration presented in Kannawadi et al. (2019) and evaluate it in narrow redshifts slices and weight it by $w' = w_s D(z_l, z_s)/D(z_s)$:

$$\bar{m} = \frac{\sum_i w'_i m_i}{\sum_i w'_i} \tag{4.8}$$

where i is the $i-$th redshift slice. The $m-$bias measured in our samples goes from -0.01 to -0.03.

4.3.1 Contamination from physically associated galaxies: boost factor and IA

Because galaxies tend to cluster and the clustering is a function of galaxy separation, there is an overdensity of sources that are physically associated with the lens. This has two implications: on one hand, these galaxies are not lensed, diluting the GGL signal at small scales; on the other hand, because these galaxies experience the local tidal field, some of them are intrinsically aligned towards the lens, that is, opposite to the lensing signal, further suppressing the signal. The former effect can be accounted by comparing the weighted number of pairs between the lens and source sample and the weighted number of pairs that a random distribution of lenses forms with the source sample, as a function of the projected separation r_p (Sheldon et al. 2004; Mandelbaum et al. 2005). This term is typically referred as boost factor:

$$B(r_\mathrm{p}) = \left.\frac{\sum_\mathrm{r} w_\mathrm{r}}{\sum_\mathrm{l} w_\mathrm{l}} \frac{\sum_\mathrm{ls} w_\mathrm{ls,eff}}{\sum_\mathrm{rs} w_\mathrm{rs,eff}}\right|_{r_\mathrm{p}} \tag{4.9}$$

where $w_\mathrm{rs,eff} = w_\mathrm{s} \left(\Sigma^{-1}_\mathrm{crit,eff}\right)^2$ and $w_\mathrm{r} = 1$.

Both the lensing dilution from unlensed galaxies and the negative contribution from IA can be removed by selecting only source galaxies that have separations larger than z_ϵ from the lens, with $z_\mathrm{s} - z_\mathrm{l} = z_\epsilon$ (Leauthaud et al. 2017). Although we also apply the boost factor, we make use of this cut when measuring the lensing signal, to ensure that any contamination is low and adopt $z_\epsilon = 0.2$.

4.3.2 Random subtraction

On top of the correction discussed in the previous section, we follow Singh et al. (2017) and subtract the signal around random points from the lensing signal. This ensures that residual additive biases, introduced by the survey edges and by the presence of masks are removed from our measurement. The random signal is obtained in exact analogy to Eq. 4.7, but measuring the lensing signal around points uniformly distributed over the survey footprint with removal of the masked regions. The final estimator is thus given by

$$\Delta\hat{\Sigma}(r_\mathrm{p}) = B(r_\mathrm{p})\Delta\hat{\Sigma}_\mathrm{ls}(r_\mathrm{p}) - \Delta\hat{\Sigma}_\mathrm{rs}(r_\mathrm{p}) \,. \tag{4.10}$$

4.3.3 Estimator for the IA signal

We are, however, also interested in measuring the IA signal of the source galaxies around the lenses. To this end, we only select galaxies within a small redshift separation from the lenses. We chose $\Delta z \equiv |z_\mathrm{l} - z_\mathrm{s}| < z_\epsilon$ with $z_\epsilon = 0.15$. The computation is analogous to the case of lensing, (Eq. 4.10): we label the resulting signal $\Delta\Sigma_{\Delta z}$ to denote the redshift range used for this measurement. The signal measured in this way is still affected by the lensing contamination, which can be removed using lensing signal measured for the 'lensing' sample. Focusing on physically associated galaxies, in this case it is crucial to correctly account for the boost factor.

The excess of lens-source pairs after the random subtraction described in the previous section causes the IA signal (as this corresponds to the clustered galaxies): the average critical surface density thus becomes:

$$\langle\Sigma_{\mathrm{crit,eff}}\rangle_{\mathrm{ex}} = \frac{\sum_{\mathrm{ls}} w_{\mathrm{ls,eff}}\Sigma^{(\mathrm{ls})}_{\mathrm{crit,eff}} - \sum_{\mathrm{rs}} w_{\mathrm{rs,eff}}\Sigma^{(\mathrm{rs})}_{\mathrm{crit,eff}}}{\sum_{\mathrm{ls}} w_{\mathrm{ls,eff}} - \sum_{\mathrm{rs}} w_{\mathrm{rs,eff}}} \,. \tag{4.11}$$

Finally, the IA estimator is (Blazek et al. 2012):

$$\hat{\gamma}_{\mathrm{IA}}(r_\mathrm{p}) = \left.\frac{\Delta\hat{\Sigma}_{\Delta z} - \Delta\hat{\Sigma}_{\mathrm{lens}}}{(B_{\Delta z} - 1)\langle\Sigma^{(\Delta z)}_{\mathrm{crit,eff}}\rangle_{\mathrm{ex}} - (B_{\mathrm{lens}} - 1)\langle\Sigma^{(\mathrm{lens})}_{\mathrm{crit,eff}}\rangle_{\mathrm{ex}}}\right|_{r_\mathrm{p}} . \tag{4.12}$$

Leonard et al. (2018) presented an improved version of this estimator which exploits the scale dependence of IA to better separate it from lensing. This requires multiple measurements of the source galaxy shapes, obtained with different shape estimates that weigh different galaxy scales differently. Here, we do not investigate this possibility, mainly motivated by the results in Georgiou et al. (2019b), who used very high S/N measurements and found that the scale dependence of IA is mainly limited to red satellites. The gain is therefore expected to be minimal in a mixed sample.

4.4 Modelling the signal with the halo model

The GGL signal captures the projected two-point correlation function between a galaxy position and a galaxy shear, which in turn is a measure of the three-dimensional correlation between matter and density distributions. Because lensing is sensitive to density contrasts, in practise we measure the difference between the projected mass density at a certain radius and the average mass density contained in that radius (eq. 4.3).

In order to model the signal, we need to provide an analytical expression for the projected surface mass density around galaxies. This is related to the three-dimensional correlation function via a projection integral. In the distant observer approximation, it can be expressed as an Abel transform

$$\Sigma(r_\mathrm{p}) = 2\bar{\rho}_m \int_{r_\mathrm{p}}^{\infty} \xi_{\delta\mathrm{g}}(r) \frac{r\,\mathrm{d}r}{\sqrt{r^2 - r_\mathrm{p}^2}} \,. \tag{4.13}$$

Here $\xi_{\delta\mathrm{g}}(r)$ is the correlation between the galaxy and the fractional matter density contrast, $\langle \delta(\mathbf{x}) \delta_\mathrm{g}(\mathbf{x}+\mathbf{r}) \rangle$, with $\delta(\mathbf{x}) = (\rho_\mathrm{X}(\mathbf{x}) - \bar{\rho}_\mathrm{X})/\bar{\rho}_\mathrm{X}$, $X \in \{\delta, \mathrm{g}\}$. In the following, we will always use the short-notation δ to indicate the dark matter and g for the galaxy. Since galaxies form inside dark matter haloes, the halo model is a natural framework to describe the matter-galaxy correlation function, $\xi_{\delta\mathrm{g}}(r)$. We present this formalism in the next section.

The projected mass contained within the radius r_p can be written as

$$\bar{\Sigma}(< r_\mathrm{p}) = \frac{2}{r_\mathrm{p}^2} \int_0^{r_\mathrm{p}} \Sigma(R') R' dR' \tag{4.14}$$

and from eq. 4.3 we can recover the ESD.

While this formalism strictly describes only the lensing effect due to the dark matter distribution, we also include the GGL due to the baryonic mass of the galaxy, here modelled as a point mass (pm),

$$\Delta\Sigma_\mathrm{pm} = \frac{\langle M_* \rangle}{\pi r_p^2} \,. \tag{4.15}$$

This approximation is motivated by the fact that the minimum scale we probe is $r_p = 60\ h^{-1}\mathrm{kpc}$, much larger than the physical extent of the stellar component of a galaxy.

We evaluate the model at the effective redshift of the lenses, z_eff, given by the weighted mean of the lenses, with weight the lensing efficiency in equation 4.6. For the `luminous` sample, this corresponds to $z_\mathrm{eff} = 0.406$, while for the `dense` sample $z_\mathrm{eff} = 0.368$.

4.4.1 The halo model

The halo model (Seljak 2000; Ma & Fry 2000; van den Bosch et al. 2013; Cooray & Sheth 2002, for a review) is a well-established formalism for predicting and interpreting the clustering and lensing statistics of galaxies and dark matter. The key idea behind the halo model is that the mass of the

halo is the fundamental property that drives halo clustering statistics. It assumes that all dark matter in the Universe is bound in haloes and that dark matter haloes are fully described by a universal density profile.

The formalism is based on a set of ingredients: a density profile for the dark matter distribution; a halo mass function, that provides a prescription of how many haloes populate a given comoving volume at a given redshift; and a halo bias function, which quantifies the bias of the bounded haloes with respect to the underlying matter distribution. Then, galaxies can be included into the formalism through a prescription that provides the way galaxies occupy dark matter haloes. The halo occupation distribution (HOD), is a convenient way of doing that, assigning the number of galaxies $N_{\rm g}$ per a give halo of mass M, $\langle N_{\rm g}|M\rangle$. We discuss in detail the model we adopt for the HOD in Sect. 4.4.3

We define dark matter haloes as spheres with an average density of 200 times the background density today, $\rho_{\rm h} = 200\rho_{\rm m}$. We assume that the dark matter is spatially distributed following the Navarro-Frenk-White profile (NFW, Navarro et al. 1996), with a concentration-mass relation from Duffy et al. (2008). We also assume that satellite galaxies are spatially unbiased with respect to the dark matter particles, i.e. that their spatial distribution is described by $\rho_{\rm s}(r, M) = \rho_{\rm h}(r, M) \equiv Mu(r, M)$, with $u(r, M)$ the normalised density profile of dark matter and r the distance from the centre of the halo. We allow central galaxies to have a different amplitude of the concentration-mass relation, which we parametrise as a free pre-factor f_c. For the halo mass function, $n(M)$, as for the halo bias function, $b_h(M)$, we adopt the functions presented in Tinker et al. (2010). We explicitly force the halo bias to be normalised at each redshift: the normalisation is obtained by integrating the halo bias function over a large range of masses ($10^2 - 10^{18}\ h^{-1}M_\odot$). We do not model the off-centering of central galaxies, i.e. we always assume that they sit at the centre of their halo.

4.4.2 The galaxy-matter power spectrum

Given a prescription for the HOD (Sect. 4.4.3) and the set of ingredients introduced in Sect. 4.4.1, it is possible to build the correlation functions between the matter density field and a continuous galaxy field, as well as their auto-correlations. As such relations involve convolutions, for computational reasons it is convenient to work in Fourier space and then transform the quantities back to real space. We thus present them in Fourier space, as they are implemented this way in the code.

One of the main advantages of the halo model is its separate treatment

of the correlation that arise between the galaxies/matter within the halo, which leads to the so called 1-halo term, and the correlation between those that belong to different haloes, the 2-halo term. As a general result, the full power spectrum is

$$P(k,z) = P^{\rm 1h}(k,z) + P^{\rm 2h}(k,z) \tag{4.16}$$

regardless whether we are describing the clustering of galaxies, of dark matter or the matter-galaxy correlation.

In turn, we can split the contributions from central and satellite galaxies and model them individually. Denoting with 'c' the central-galaxy components, with 's' the terms which are sourced by the satellite population, and with δ those corresponding to matter, we have that any correlation is given by the sum of all of the possible correlations between these terms. In Fourier space, for the case of the galaxy-matter cross power spectrum, this reads:

$$P_{{\rm g}\delta}(k,z) = f_{\rm c} P^{\rm 1h}_{{\rm c}\delta}(k,z) + f_{\rm s} P^{\rm 1h}_{{\rm s}\delta}(k,z) + f_{\rm c} P^{\rm 2h}_{{\rm c}\delta}(k,z) + f_{\rm s} P^{\rm 2h}_{{\rm s}\delta}(k,z)\ . \tag{4.17}$$

Here f_X with $X \in \{{\rm c}, {\rm s}\}$ is the fraction of galaxies of a given type entering the correlation. These can be obtained from the galaxy number densities as predicted by the HOD as

$$f_X = \frac{n_X}{n_{\rm g}}\ , \tag{4.18}$$

where

$$n_X = \int_0^\infty \langle N_X | M \rangle\ n(M)\ {\rm d}M\ . \tag{4.19}$$

It is convenient to introduce the functions $\mathcal{H}_X$, where $X = \{\delta, {\rm c}, {\rm s}\}$ and are thus associated to a given component:

$$\mathcal{H}_\delta(k,M) = \frac{M}{\rho_{\rm m}} u(k,M)\ , \tag{4.20}$$

$$\mathcal{H}_{\rm c}(k,M) = \frac{\langle N_c | M \rangle}{n_g} \tag{4.21}$$

and

$$\mathcal{H}_{\rm s}(k,M) = \frac{\langle N_s | M \rangle}{n_g} u(k,M)\ . \tag{4.22}$$

The 1-halo and 2-halo terms of the power spectrum thus read:

$$P^{1h}_{xy}(k) = \int_0^\infty \mathcal{H}_x(k,M) \mathcal{H}_y(k,M)\ n(M)\ {\rm d}M \tag{4.23}$$

and

$$P_{xy}^{2h}(k) = P_{\rm lin}(k) \int_0^\infty {\rm d}M_1 \, \mathcal{H}_x(k, M_1) b_{\rm h}(M_1) n(M_1) \times \int_0^\infty {\rm d}M_2 \, \mathcal{H}_y(k, M_2) b_{\rm h}(M_2) n(M_2) \, . \tag{4.24}$$

A relevant quantity that we can predict via this formalism is the average mass mass of bounded haloes that host a central galaxy. This is defined as:

$$\langle M_{200} \rangle = \frac{1}{n_{\rm c}(z_{\rm eff})} \int \langle N_{\rm c} | M \rangle n(M) M {\rm d}M \, . \tag{4.25}$$

4.4.3 The halo occupation distribution

Following Cacciato et al. (2009), we derived the HOD from the Conditional Luminosity Function (CLF) obtained for the SDSS by Yang et al. (2003). The CLF, $\mathrm{d}\Phi(L|M)\mathrm{d}M$, specifies the average number of galaxies with luminosity in the range $L \pm \mathrm{d}L/2$ that reside in a halo of mass M. Thus, integrating over a certain luminosity bin provides the number of galaxies with a certain luminosity $L \in [L_1, L_2]$ that reside in a halo of mass M,

$$\langle N_g | M, L_1, L_2 \rangle = \int_{L_1}^{L_2} \Phi(L|M) {\rm d}L \tag{4.26}$$

As in Cacciato et al. (2009), we split the CLF in two components,

$$\Phi(L|M) = \Phi_{\rm c}(L|M) + \Phi_{\rm s}(L|M), \tag{4.27}$$

where $\Phi_{\rm c}(L|M)$ is the CLF associated with central galaxies, while $\Phi_{\rm s}(L|M)$ is the CLF associated with satellite galaxies.

The central galaxy CLF is described by a log-normal function,

$$\Phi_{\rm c}(L|M) dL = \frac{\log e}{\sqrt{2\pi}} \exp\left[-\frac{(\log L - \log L_{\rm c})^2}{2\sigma_{\rm c}^2} \right] \frac{{\rm d}L}{L}, \tag{4.28}$$

where

$$L_{\rm c}(M) = L_0 \frac{(M/M_1)^{\gamma_1}}{[1 + (M/M_1))^{\gamma_1 - \gamma_2}]} \tag{4.29}$$

is the mean luminosity of central galaxies in a halo of mass M. M_1 is the characteristic mass scale at which $L_{\rm c}(M)$ changes its slope ($L_{\rm c} \propto M^{\gamma_1}$ for $M \ll M_1$ and $L_{\rm c} \propto M^{\gamma_2}$ for $M \gg M_1$). Eq. 4.29 is one of the key relations we aim to constrain for the LRG sample (see Sec. 4.6).

Satellite galaxies obey

$$\Phi_{\rm s}(L|M) = \Phi_{\rm s}^* \left(\frac{L}{L_s^*}\right)^{\alpha_{\rm s}+1} \exp\left[-\left(\frac{L}{L_{\rm s^*}}\right)^2\right] \frac{{\rm d}L}{L}, \tag{4.30}$$

where $L_{\rm s^*}(M) = 0.562 L_{\rm c}(M)$ and

$$\log[\Phi_{\rm s}^*(M)] = b_0 + b_1(\log M_{12}) \tag{4.31}$$

In total, our halo occupation distribution is described by nine parameters: $\log M_1, \log L_0, \gamma_1, \gamma_2, \sigma_{\rm c}, f_{\rm c}\alpha_{\rm s}, b_0, b_1$.

4.5 Fitting procedure

We sample the parameter space via a Monte Carlo Markov Chain procedure, using the Emcee sampling[3] (Foreman-Mackey et al. 2013) sampler. We assume a Gaussian Likelihood of the form

$$\mathcal{L} \propto \exp\left[-\frac{1}{2}(\mathbf{D}_i - \mathbf{M}(\theta)_i)^{\rm T} \mathbf{C}_{ij}^{-1} (\mathbf{D}_j - \mathbf{M}(\theta)_j)\right], \tag{4.32}$$

where $\mathbf{D}$ is the data vector, $\mathbf{M}(\theta)$ is the model evaluated for the set of parameters θ, and i, j refer to the radial bin under consideration, and $\mathbf{C}_{ij}^{-1}$ is the inverse of the data covariance matrix. We employ 120 walkers and check the convergence of the chains by visually inspecting the chains. The priors for the HOD parameters are reported in Table 4.1 and are based on previous results in literature. In particular, while we broadly follow the choice of the priors in Bilicki et al. (2021), we adopt more informative priors in the following cases: $\sigma_{\rm c}$ has been shown to be tightly constrained by current measurements as investigated in Cacciato et al. (2014, see e.g. their Fig. 6); γ_1 is expected to be poorly constrained by a luminous sample such as the LRGs: here we follow Cacciato et al. (2014), but rather than fixing it we provide an informative prior centred on the best-fit value in C13; the prior for γ_2 is typically extremely broad: however, the best-fit values obtained for different samples are all in good agreement and span the range $0.2 - 2.0$ (Cacciato et al. 2013, 2014; van Uitert et al. 2016a; Dvornik et al. 2018; Bilicki et al. 2021): we thus restrict the sample to the range $\mathcal{U}(0, 2)$. We also reduce the range of $f_{\rm c}$ based on some preliminary runs and exclude zero to avoid unphysical behaviour of the model.

[3] `https://emcee.readthedocs.io/en/stable/`

Table 4.1: The priors adopted in the fit and the corresponding fiducial values, here reported as the median of the marginal posteriors, while the best fit values are reported in brackets. The error bars correspond to the 16th and 84th percentiles. $\mathcal{N}(\mu, \sigma)$ indicates a normal distribution with mean μ and standard deviation σ.

Parameter	Prior	Fiducial
f_c	$[0.1, 1]$	$0.977^{+0.017}_{-0.054}$ (0.999)
$\log(L_0/[h^{-2}L_\odot])$	$[7, 13]$	$9.950^{+0.331}_{-0.577}$ (10.357)
$\log(M_1/[h^{-1}M_\odot])$	$[9.0, 14.0]$	$11.656^{+0.341}_{-0.434}$ (12.070)
γ_1	$\mathcal{N}(3.18, 2)$	$4.224^{+1.888}_{-1.863}$ (3.146)
γ_2	$[0, 2]$ (0.266)	$0.421^{+0.174}_{-0.140}$ (0.266)
σ_c	$[0.1, 0.3]$	$0.131^{+0.060}_{-0.022}$ (0.115)
α_s	$\mathcal{N}(-1.1, 0.9)$	$-1.734^{+0.524}_{-0.404}$ (-1.478)
b_0	$\mathcal{N}(0, 1.5)$	$-1.355^{+0.491}_{-0.456}$ (-1.607)
b_1	$\mathcal{N}(1.5, 2.0)$	$0.864^{+0.287}_{-0.359}$ (1.056)

4.6 Constraints on the lens sample properties

We measured the ESD signal of the `dense` and `luminous` samples in bins in luminosity, applying the cuts presented in Fortuna et al. (2021b) and labelled `D1, D2, D3, D4, D5, L1, L2, L3`. The `D1` and `L1` samples of this studies slightly differ from those in Fortuna et al. (2021b), because of the removal of the galaxies that reside in the tails of the distributions[4]. Removing the tail is crucial for the correct interpretation of the luminosity distributions by the model: the HOD modelling assumed here is designed for volume-complete samples. Given the lack of a selection function in the model, the long faint-tail would be populated by a large number of faint galaxies, as predicted by the modified Schechter function in Eq. 4.30. We explore how well our model can capture the luminosity distribution of our samples in Appendix A1.

The properties of the lens samples are reported in Table 4.2. We jointly fit all the samples with a single model and found a unique set of HOD parameters, which we report in Table 4.1. The reduced χ^2 is 1.05.

The best-fit HOD parameters agree within the error bars with the best-fit parameters of the red population of the KiDS-Bright sample (Bilicki et al. 2021). This is a sign that the two samples, albeit selected with different

[4]The tail is due to the photo-z scatter, such that a $m_r(z)$ cut does not translate into a sharp cut in absolute magnitudes. We also remove part of the high-L, with a cut at $M_r - 5\log(h) = -22.6$.

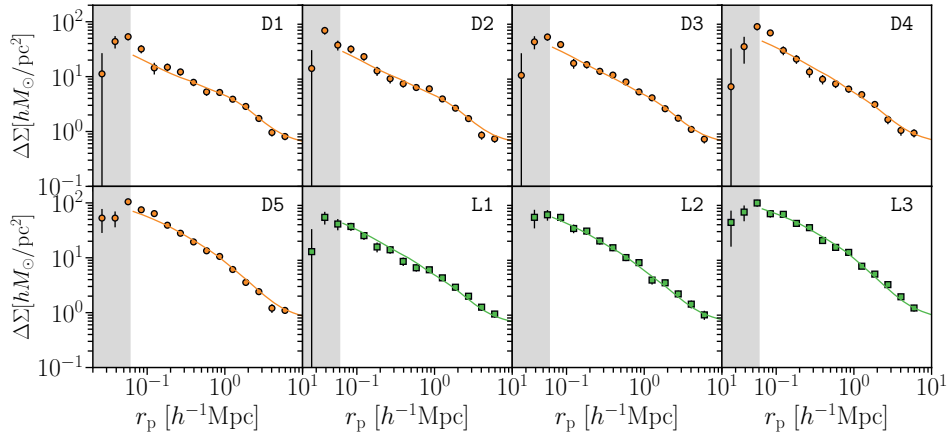

Figure 4.2: The ESD measurements for the samples listed in Table 4.2. We plot the best fit curves (Table 4.1) on top of the data points. The grey shadowed area is excluded from the fit. The reduced χ^2 of the fit is $\chi^2_\mathrm{red} = 1.05$.

cuts, are characterised by similar scaling relations. It is, however, surprising that the stellar-to-halo mass relation of the red galaxies of the Bright sample has a very similar scaling to the luminosity-to-halo mass relation of the LRG sample (see Sect. 4.6.1). We interpret this result as a consequence of the observed luminosity-to-stellar mass-relation for the LRGs, which is close to unity (see Tab. 4.2).

4.6.1 Luminosity-halo mass relation

For each sample, we derive the corresponding average halo mass, $\langle M_{200}\rangle$ (Eq. 4.25). These are reported in Table 4.2. At intermediate luminosity (`D5, L2 L3`), our results are in good agreement with previous studies (Mandelbaum et al. 2006; Miyatake et al. 2015; van Uitert et al. 2015), although at high luminosity the extrapolation of our best-fit curve is above the measurements from literature. Here, we only show the point from van Uitert et al. (2015) which are the closest to the effective redshift of our samples. We also note that Mandelbaum et al. (2006) use a different definition of halo mass, and thus the comparison has to be considered only qualitative. However, our samples are overall fainter than these, providing an extension to the $L - M$ towards lower luminosities. This is illustrated in Fig. 4.3, where we also plot the luminosity-halo mass relation for the central galaxies as predicted in Eq. 4.29. Given that the fraction of satellites is overall low (see Table 4.2), the qualitative agreement between the data

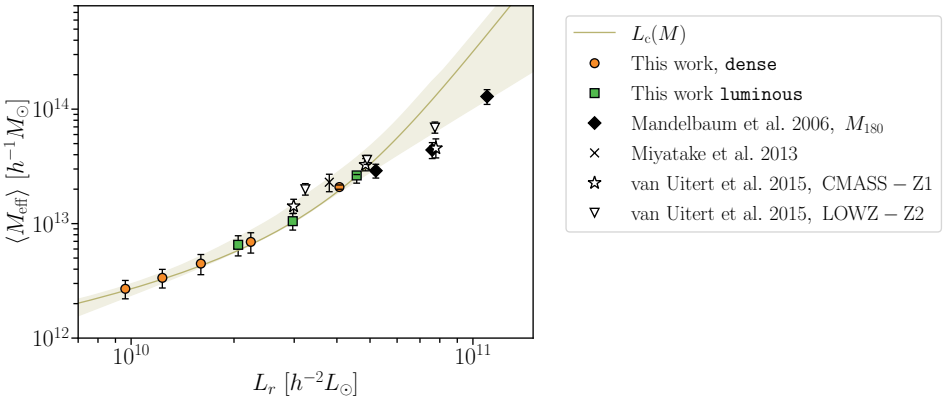

Figure 4.3: The luminosity-halo mass relation for the LRG sample (`dense` orange circles; `luminous` green squares), compared with similar measurements from different sample in the literature. The solid line shows the $L_c(M)$ relation predicted by our model.

Table 4.2: Properties of the lens samples.

Sample	$\langle \log L[h^{-2}L_\odot]\rangle$	$\langle \log M_*[h^{-2}M_\odot]\rangle$	$\langle \log M_{200}[h^{-1}M_\odot]\rangle$	f_s
D1	10.01	10.25	12.43 ± 0.05	0.29 ± 0.05
D2	10.20	10.35	12.53 ± 0.06	0.27 ± 0.04
D3	10.21	10.46	12.65 ± 0.07	0.24 ± 0.03
D4	10.35	10.62	12.84 ± 0.08	0.2 ± 0.02
D5	10.59	10.84	13.32 ± 0.03	0.13 ± 0.01
L1	10.33	10.63	12.81 ± 0.08	0.19 ± 0.02
L2	10.48	10.77	13.02 ± 0.07	0.16 ± 0.02
L3	10.65	10.94	$13.42^{+0.02}_{-0.05}$	0.11 ± 0.02

$\langle M_{200}\rangle$ and f_s are derived from the set of HOD parameters that maximise the likelihood. The error bars correspond to the 16th and 84th percentiles.

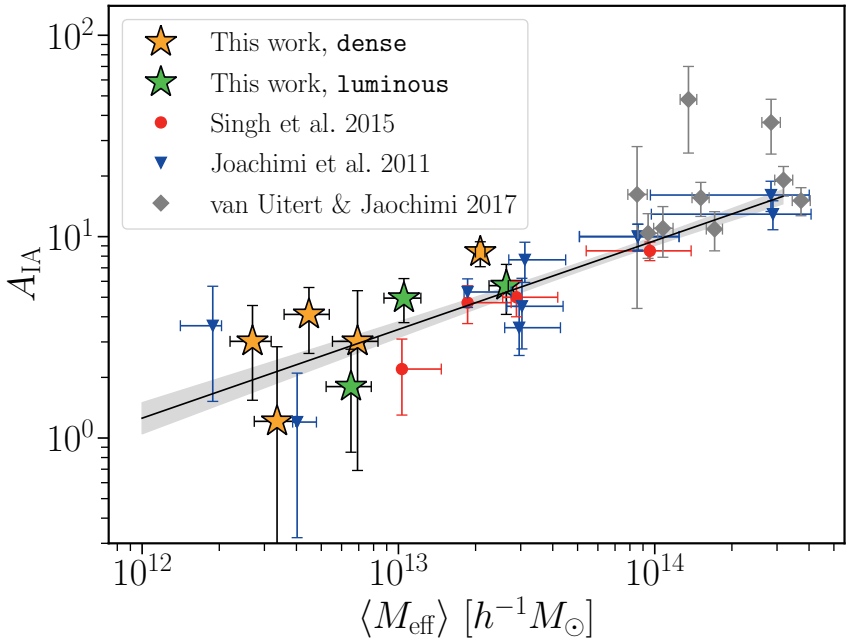

Figure 4.4: The dependence of IA on halo mass for different IA measurements. The halo masses, $\langle M_{\rm eff}\rangle$, are obtained as described in the text. We indicate our measurements with star markers (orange: `dense` sample, green: `luminous`); the other data points are taken from the literature. The solid black line shows the best fit curve of the $A_{\rm IA}(M)$ relation described by Eq. (4.33), while the shaded area delimits the 68% confidence region.

and the curve is expected and the curve provides a useful comparisons for simulations and the galaxy properties in mock catalogues.

4.6.2 IA dependence on halo mass

To explore the implications of the observed luminosity-to-halo mass relation for the IA signal of the LRGs, we use the measurements in Fortuna et al. (2021b) and place them into context using the estimates of the halo masses obtained in the previous section. Fortuna et al. (2021b) used a Non-Linear Linear Alignment model (Hirata & Seljak 2004; Bridle & King 2007), adapted to account for the photometric redshift uncertainty (Joachimi et al. 2011), to fit the IA signal at large scales ($r_{\rm p} > 6\,h^{-1}{\rm Mpc}$). The best-fit IA amplitudes, $A_{\rm IA}$, of the different sub-samples are shown in Fig. 4.4 as orange (`dense`) and green (`luminous`) stars.

When combined with previous measurements in the literature, Fortuna

et al. (2021b) found that the IA dependence of the red galaxies can be described well by a double power law, with a break at $L_r \lesssim 3.2 \times 10^{10} h^{-2} L_{r,\odot}$, although the data show a large scatter at low-L. We are now in a position to investigate whether this dependence was primarily sourced by the halo mass, or if the relation is more complex and requires the addition of secondary galaxy properties. Interestingly, our measurements of $L(M)$ lie on the transition between the two regimes of the power law in Eq. 4.29. This means that the double power law in the IA-L plane reflects at least partially the double power law in the $L - M$ plane. We explore this further by showing the IA amplitudes in Fortuna et al. (2021b) as a function of weak lensing mass in Fig. 4.4. Although the scatter is too large to draw definitive conclusions, we note that the overall trend matches a single power law. To obtain a more complete picture, we also added the measurements from Joachimi et al. (2011) (MegaZ, SDSS LRGs, the L3 and L4 samples from the SDSS) and Singh et al. (2015) (LOWZ) to Fig. 4.4, which are based on LRGs and thus can safely be assumed to be mainly centrals[5] To do so, we converted the luminosity of each sample into an estimate of their halo mass, via the relation found in Sect. 4.6 and displayed in Fig. 4.3. Singh et al. (2015) provide estimates of the halo masses of their samples, but those are based on a different definition of halo mass and for ease of comparison we decided to use our scaling relation. Since van Uitert & Joachimi (2017) do not provide the luminosity of the clusters, but use the same definition of halo mass, we decided to use their halo mass estimate. We fit all the measurements in Fig. 4.4 with a single power law of the form:

$$A_{\rm IA}(M) = A \left(\frac{M}{M_0} \right)^{\beta_M} , \tag{4.33}$$

with $M_0 = 10^{13.5} h^{-1} M_\odot$. We find a best fit amplitude of $A = 5.74^{+0.32}_{-0.32}$ and slope $\beta_M = 0.44^{+0.04}_{-0.04}$. The reduced χ^2 is 1.64 for 21 degrees of freedom. We stress, however, that some of the masses associated to these measurements lie beyond the range constrained by our data, and are thus an extrapolation. This is relevant because a small variation of the slope becomes significant at high–L. We test the impact of this by replacing our $L - M$ relation with the one in van Uitert et al. (2015) for the high-mass points (LOWZ, MegaZ and SDSS LRGs). This relation was also adopted in Piras et al. (2018) and includes a redshift dependence, which we do not consider in our model. When repeating the fit with this new set of data, we still find comparable

[5]For this reason, we decided to omit the measurements from Johnston et al. (2019), which are known to have a larger fraction of satellites.

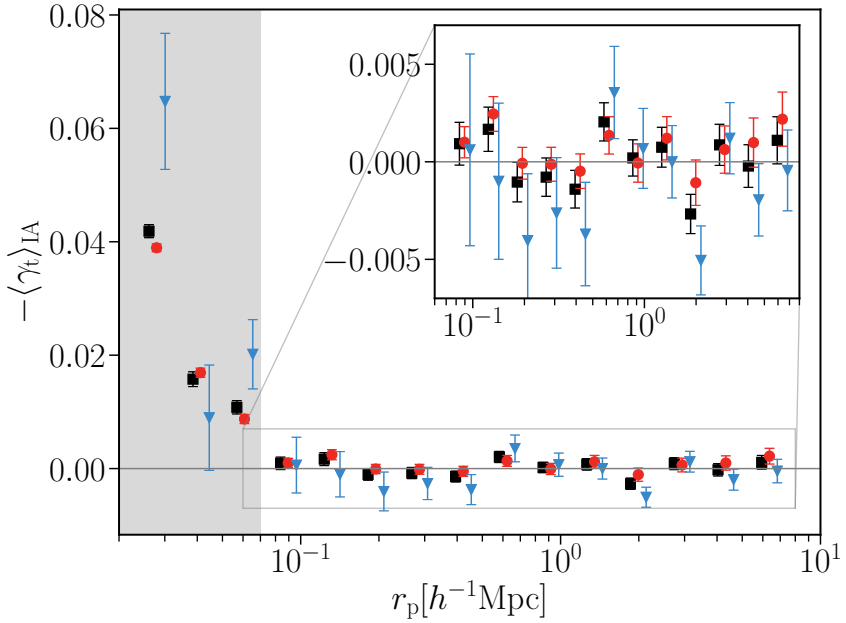

Figure 4.5: The IA signal of the source galaxy sample around the LRGs, selected for small redshift separations ($|z_l - z_s| < 0.15$). We consider the signal from the full source sample (black squares), and its split in red/blue (red circles/blue triangles). At separations below $0.06\ h^{-1}\mathrm{Mpc}$ (grey region) blending becomes important and thus we do not consider it in the analysis. For clarity, the red and blue points are shifted horizontally.

results within the model uncertainty although we notice an improvement in the reduced χ^2, which in this case is 1.19. We also tested the impact of the clustering measurements on our fit: the interpretation of their IA signal is indeed complicated by the fact that their shapes are obtained with a different technique than for the LRG samples (van Uitert & Joachimi 2017). We thus removed them from our data vector and repeated the fit: the result of this test is compatible with our fiducial setup.

4.7 Constraints on the IA of the source sample

To constrain the IA of the source galaxies we measured the $\langle\gamma_t\rangle$ signal in narrow bins in redshift ($\Delta z \equiv |z_l - z_s| = 0.15$)[6] and subtracted the lens-

[6]We note that with this definition, the galaxy-galaxy separation is a function of redshift. Here, we are primarily limited by the photometric redshift uncertainty, and thus consider

ing contribution as described in Sect. 4.3.3[7]. Selecting only galaxies with a small separation along the line-of-sight enhances the IA signal, while removing a substantial part of the lensing contribution. The different choice in z-binning is fully accounted for in the model through $\Sigma_{\rm crit}$, which is computed according to the new galaxy selection. The average signal, $\langle\gamma_{\rm t}(r_{\rm p})\rangle$ is computed as in Eq. 4.12 and thus is the average tangential ellipticity $\epsilon_{\rm t}$, weighted by the lensing efficiency. Hence, the IA signal is expressed in terms of the weighted intrinsic shear instead of the intrinsic ellipticity, as in Georgiou et al. (2019b).

Here, we only consider the lens galaxies from the `dense` sample, without any split in luminosity. In Appendix A2 we report the fraction of galaxies of the source sample that are physically associated to the LRGs. The results are presented in Fig. 4.5. We do not detect any intrinsic alignment for the full source sample, $\langle\gamma_{t,\rm IA}\rangle = -0.0001$ up to $10\,h^{-1}{\rm Mpc}$, with a χ^2 of the null-hypothesis of $\chi^2_{\rm null} = 1.67$. As for the GGL signal, we do not consider the data points below $0.06\ h^{-1}{\rm Mpc}$, where observational systematics become important. Although at small scales IA is expected to be radial dependent (Pereira et al. 2008; Pereira & Bryan 2010), having detected zero signal, we limit our fit to a constant value and do not consider more sophisticated models: we find $C = (-0.49 \pm 1.4) \times 10^{-4}$.

We explore now the possibility that the signal is washed out by the presence of blue galaxies in the sample, which are expected to be poorly or none aligned. We thus split the source galaxies based on their morphology. We follow Li et al. (2021) and use the parameter $T_{\rm B}$ from the BPZ photo-z code (Benítez 2000; Coe et al. 2006) as a proxy for the morphology: we identify the 'red' population (a combination of E1, Sbc, Scd types) as the galaxies satisfying $T_{\rm B} \leqslant 3$, while the 'blue' one is the complementary sample, selected by requiring $T_{\rm B} > 3$. The signal is displayed in Fig. 4.5. Also in this case we do not observe any alignment signal, with $\langle\gamma_{t,\rm IA}^{(\rm red)}\rangle = -0.0007$ ($\chi^2_{\rm null,red} = 1.39$) and $\langle\gamma_{t,\rm IA}^{(\rm blue)}\rangle = 0.0011$ ($\chi^2_{\rm null,blue} = 1.35$). We also report the best fit values of the constant fit, which in this cases are: $C^{(\rm red)} = -0.0003 \pm 0.0002$ and $C^{(\rm blue)} = 0.0003 \pm 0.0002$.

To measure the IA with the split in colour, we subtracted the same lensing signal as for the full sample. This is motivated by the fact that lensing does not depend on the source galaxy colour. We tested, however, that the residual IA that might contaminate the signal did not affect the results by

this effective treatment as sufficient.

[7]We stress that this IA signal differs from the one discussed in the previous section, which was obtained by using the two-point projected correlation function.

measuring the lensing signal only for the red source galaxies and measured the IA by subtracting this 'red lensing' ESD from $\Delta\Sigma^{(\mathrm{red})}_{\Delta z}$. We found the results to be compatible within the statistical uncertainty with our fiducial setup.

Our results are in line with previous measurements (Hirata & Seljak 2004; Blazek et al. 2012; Chisari et al. 2014; Sifón et al. 2015). Dark matter only simulations predict satellite galaxies to be radially aligned towards the centre of the halo (Pereira et al. 2008; Pereira & Bryan 2010), but this signal is significantly washed out when considering the stellar component (Velliscig et al. 2015b), as a possible consequence of the misalignment between the luminous and the dark component of the galaxy (Velliscig et al. 2015a). Pereira & Kuhn (2005) and Faltenbacher et al. (2007) both detected a radial alignment signal, the fist in cluster galaxies and the second on red satellites in the SDSS galaxy group catalogue (Yang et al. 2007). In line with these findings, recently, Georgiou et al. (2019b) detected a radial signal for both red and blue satellites in galaxy groups selected from the Galaxy And Mass Assembly survey (GAMA, Driver et al. 2009). However, all of these studies rely on spectroscopic redshifts, and thus to a more robust assignment of the galaxies to their group: here, we considered all galaxies within a given redshift separation, which significantly degrades the signal. The uncertainty in photometric redshifts also contributes to dilute the signal due to the promotion of uncorrelated pairs within the selection as well as the removal of physically associated galaxies. Moreover, Velliscig et al. (2015a) find that IA depends on the subset of stars used to the signal: using all the stars bound in sub-haloes, the signal is significantly increased compared to the alignment of stars within the half-mass radius. In this latter case, they find compatible values for $\langle \epsilon_{\mathrm{g}+} \rangle$ to Chisari et al. (2014); Sifón et al. (2015); Singh et al. (2015). This is in line with the finding in Georgiou et al. (2019b) that the alignment signal is a function of galaxy scale, with the outskirt of the galaxy being more aligned with the position of the central galaxy. In this sense, *lens*fit, which weighs more the inner part of the galaxy, might also contribute to the low signal observed in our samples.

4.8 Conclusions

We used weak gravitational lensing to measure the mass of a sample of LRGs for which the IA signal was measured in Fortuna et al. (2021b). We split the sample into bins based on their luminosity, and used a halo model to interpret our data. We fit the ESD measurements of all the luminos-

ity bins jointly, with a single model. We confirmed that the LRG sample consists mainly of central galaxies, as expected for this kind of galaxy population, and provide the satellite fraction for each L−bin. We ensured that the modelling recovers the true galaxy properties sufficiently well, by inspecting the luminosity distribution per each luminosity bin predicted by the model: we find good agreement between the predicted and the real distributions.

The best fit model predicts an increasing average halo mass with luminosity, which we model with a double power law, for which we obtain the following slopes: $\gamma_1 = 4.412$ and $\gamma_2 = 0.476$ (Eq. 4.29). We note, however, that our data mainly constrain the high mass-end of the double power law ($M > M_1$), which is reflected by the uncertainties in γ_1. Our results are in good agreement with previous studies at high luminosity and extend the luminosity-to-halo mass relation towards the faint-end (low mass).

We used these results to interpret the IA dependence with halo mass, starting from the luminosity dependence measured in the literature. The IA-halo mass relation can be parametrised by a single power law, as predicted by current models (Piras et al. 2018). This suggests that the flattening at low luminosity, hinted at by Fortuna et al. (2021b), may be caused by the double power law in the luminosity-to-halo mass relation. Although the scatter in the measurements remains large, this would imply that the halo mass is the driving source of the alignment.

We also measured the IA signal of the lensing source sample around the LRGs, by selecting only pairs with a maximum separation of $|z_\mathrm{l} - z_\mathrm{s}| = 0.15$. We considered three cases: the full source sample, and a split in red and blue. We did not detect any alignment signal, in none of the cases considered for $r_\mathrm{p} > 0.06\,h^{-1}\mathrm{Mpc}$. We mainly attribute our null-detection to the photometric redshift selection of the galaxy pair: the use of better photo-z might revisit our conclusions.

Acknowledgements

MCF and HH acknowledge support from Vici grant 639.043.512, financed by the Netherlands Organisation for Scientific Research (NWO). HH also acknowledges funding from the EU Horizon 2020 research and innovation programme under grant agreement 776247. AD acknowledges support from the European Research Council under grant agreement No. 770935.

Based on data products from observations made with ESO Telescopes at the La Silla Paranal Observatory under programme IDs 177.A- 3016,

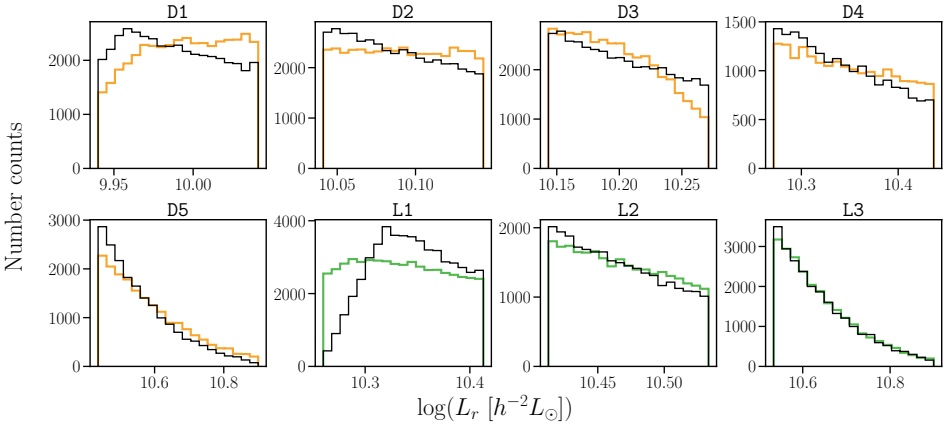

Figure 6: The real data number counts per luminosity bin (`dense`: orange, `luminous`:green) and the prediction from the best-fit model (black), normalised for the number of objects in the given bin.

177.A-3017 and 177.A-3018, and on data products produced by Tar- get/ OmegaCEN, INAF-OACN, INAF-OAPD and the KiDS production team, on behalf of the KiDS consortium. OmegaCEN and the KiDS production team acknowledge support by NOVA and NWO-M grants. Members of INAF-OAPD and INAF-OACN also acknowledge the support from the Department of Physics & Astronomy of the University of Padova, and of the Department of Physics of Univ. Federico II (Naples).

Author contributions: All authors contributed to the development and writing of this paper. The authorship list is given in three groups: the lead authors (MCF, HH, AD) followed by two alphabetical groups. The first alphabetical group includes those who are key contributors to both the scientific analysis and the data products. The second group covers those who have either made a significant contribution to the data products, or to the scientific analysis.

A1 How well does the model predict the luminosity distribution of the galaxies?

The HOD modelling adopted in this work relies on the relation between the halo mass and the luminosity of the galaxies that populate it via the CLF. This allows us to test how well the best-fit model recovers the luminosity distributions of the galaxy samples, a quantity which is not directly used

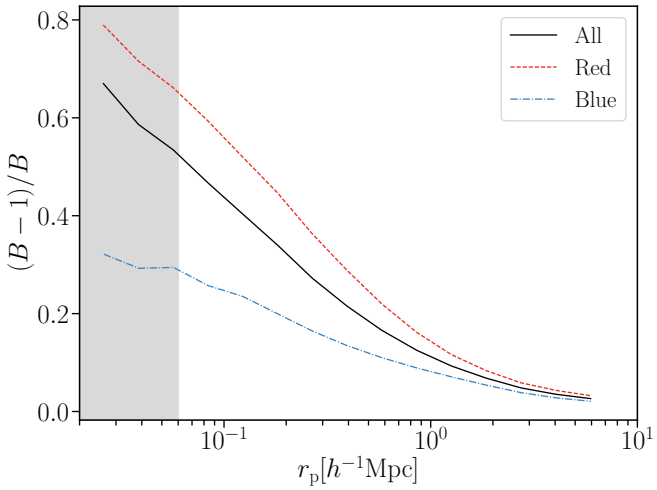

Figure 7: The fraction of source galaxies that are physically associated to the LRGs.

in the fit. This represents an independent test of the ability of the model to recover the properties of the lens galaxies. Fig. 6 shows our results. We use the predicted luminosity function (LF) at the $z_{\rm eff}$ of the corresponding sample to generate the model distributions (black solid line), while the orange/green lines show the underlying true number counts. Overall, the model reproduces sufficiently well the galaxy distribution per luminosity bin, with the exception of L1, where the distribution is significantly more peaked than the real one.

A2 Fraction of physically associated galaxies

In this Appendix we report the fraction of galaxies of the different source samples (all/red/blue) that are physically associated to the LRGs. The fractions are presented in Fig. 7 as a function of projected separation, and they are computed as $(B(r_{\rm p})-1)/B(r_{\rm p})$.